Color-gradient-based phase-field equation for multiphase flow

Reza Haghani [1], Hamidreza Erfani [1], James E. McClure,[2] Eirik Grude Flekkøy [3], and Carl Fredrik Berg [1,*]

[1]*PoreLab, Department of Geoscience and Petroleum, Norwegian University of Science and Technology (NTNU), 7031 Trondheim, Norway*

[2]*National Security Institute, Virginia Tech, RB1311 Research Center Drive, Blacksburg, Virginia 24061, USA*

[3]*PoreLab, the Njord Center, Department of Physics, University of Oslo, 0371 Oslo, Norway*

(Received 27 April 2023; accepted 22 January 2024; published 8 March 2024)

In this paper, the underlying problem with the color-gradient (CG) method in handling density-contrast fluids is explored. It is shown that the CG method is not fluid invariant. Based on nondimensionalizing the CG method, a phase-field interface-capturing model is proposed which tackles the difficulty of handling density-contrast fluids. The proposed formulation is developed for incompressible, immiscible two-fluid flows without phase-change phenomena, and a solver based on the lattice Boltzmann method is proposed. Coupled with an available robust hydrodynamic solver, a binary fluid flow package that handles fluid flows with high density and viscosity contrasts is presented. The macroscopic and lattice Boltzmann equivalents of the formulation, which make the physical interpretation of it easier, are presented. In contrast to existing color-gradient models where the interface-capturing equations are coupled with the hydrodynamic ones and include the surface tension forces, the proposed formulation is in the same spirit as the other phase-field models such as the Cahn-Hilliard and the Allen-Cahn equations and is solely employed to capture the interface advected due to a flow velocity. As such, similarly to other phase-field models, a so-called mobility parameter comes into play. In contrast, the mobility is not related to the density field but a constant coefficient. This leads to a formulation that avoids individual speed of sound for the different fluids. On the lattice Boltzmann solver side, two separate distribution functions are adopted to solve the formulation, and another one is employed to solve the Navier-Stokes equations, yielding a total of three equations. Two series of numerical tests are conducted to validate the accuracy and stability of the model, where we compare simulated results with available analytical and numerical solutions, and good agreement is observed. In the first set the interfacial evolution equations are assessed, while in the second set the hydrodynamic effects are taken into account.

DOI: 10.1103/PhysRevE.109.035301

I. INTRODUCTION

Multiphase phenomena occur frequently both in nature and industrial processes, with applications in engineering and science such as microfluidic devices [1], inkjet printing [2], fluid flows in porous media [3,4], CO_2 storage [5], etc. Over the past years, there have been numerous attempts to model multiphase fluid flow numerically, which has led to a range of different methods. The resulting methodologies of direct numerical simulations can be categorized as either sharp-interface or diffuse-interface methods [6,7].

The lattice Boltzmann method (LBM), as an alternative to the classical computational fluid dynamics (CFD), has emerged as a versatile method, capable of handling different types of physics [8–10]. Based on this method, several single-phase and multiphase models have been proposed. Different multiphase methods include the color-gradient (CG) model [11], the Shan and Chen (SC) model [12,13], the free energy model [14], and the mean-field model [15].

The CG model was first proposed by Gunstensen *et al.* [11] based on the lattice gas model of Rothman and Keller [16]. The original model has a perturbation step that realizes the surface tension between the two fluids, and a recoloring step to separate them. The model was later modified by Grunau *et al.* [17] to handle fluid flows with small density and viscosity contrasts. In their model, the squared of the sound speed ratio is the inverse of the density ratio which hinders the model from solving fluid flows with large density contrast. Lishchuk *et al.* [18] modeled interfacial tension by using the continuum surface force (CSF). In their model, the perturbation step in the Gunstensen *et al.* [11] model is replaced by a force term acting in the interface region. Latva-Kokko and Rothman [19] proposed a recoloring step to tackle the lattice pinning behavior of the Gunstensen *et al.* [11] model. A perturbation operator responsible for generating surface tension force was proposed by Reis and Phillips [20] based on its mechanical definition in two-dimensional (2D) systems. Then, this scheme was extended to three-dimensions (3D) by Liu *et al.* [21]. Both 2D and 3D models suffer from the lack of Galilean invariance [22]. Huang *et al.* [23] showed that in the former models, there are unwanted terms in the recovered macroscopic equations using the Chapman-Enskog (CE) analysis. These terms significantly reduce the accuracy of results for fluid flows with density contrast. They proposed a scheme for tackling the problem which works for fluid pairs

*Author to whom correspondence should be addressed: carl.f.berg@ntnu.no

with density contrasts up to 10 [23]. By removing the error terms in the momentum equations based on the approach of Li *et al.* [24], Ba *et al.* [25] and then Wen *et al.* [26] developed a 2D model and a 3D color-gradient model, respectively. The two aforementioned models are restricted to density ratios up to 100. Moreover, the surface tension is determined based on two free parameters. Lafarge *et al.* [27] proposed an equation of state (EOS) based on the stiffened gas formulation which relieves the density ratio problem of Grunau [17] with additional variables. The CG method has been developed to incorporate different physics. For example, Akai *et al.* [28] developed a boundary condition for complicated 3D geometry. They showed that the commonly used boundary condition, known as the fictitious boundary condition [29], sometimes leads to inaccurate results. Montessori *et al.* [30,31] developed an LB model by augmenting the stress-jump condition across the interface with a repulsive term in order to provide a mesoscale representation of all the repulsive near-contact forces. Using this coarse-grained approach, they simulated colliding droplets, a dense emulsion in microchannels, and soft-flowing crystals in microfluidic focusers.

A further look into the macroscopic equivalent of the lattice Boltzmann (LB) CG method, with the modified recoloring step of Halliday's model [32] and by treating the perturbation step in a CSF manner [18], reveals that this method can be interpreted as a phase-field method which mostly resembles the Allen-Cahn (AC) equation. Subhedar [33] developed a CG lattice Boltzmann model in which the mobility is related to the hydrodynamic pressure and density field. They mentioned that fluctuation of the hydrodynamic pressure is in the order of squared Mach number (Ma) and changes slightly during simulations. They also calculate the phase field (order parameter), which is an indicator of the interface, from the fluid population of one fluid, which is in contrast with the nature of the CG method in which two fluid populations determine the location of the interface.

Considering the previous studies, this paper aims to develop a formulation of the CG model addressing the above-mentioned difficulties. Two phase fields are solved and based on them the density is determined. The model is solved by lattice Boltzmann equations (LBEs) coupled with an available robust LBE for the hydrodynamic equation [34].

The rest of the paper is organized as follows. In Sec. II, we first develop a formulation based on the CG model. Then, an LB model is developed which comprises three distinct distribution functions. Two of these are employed to recover the macroscopic interfacial evolution equations, while the last one is utilized to recover the hydrodynamic properties. In Sec. III, numerical results and validation are presented. We will validate the model based on simulations of interface-capturing benchmarks such as diagonal translation of a circular interface, rotation of Zalesak's disk, circular interface in a shear flow, deformation of a circular interface, and on hydrodynamic benchmarks such as the Laplace test, the Rayleigh-Taylor instability, and droplet splashing on a thin liquid film. These validation cases demonstrate that the approach is able to accurately capture complex multiphase flow phenomena that present challenges for other lattice Boltzmann formulations. A summary and concluding remarks are provided in Sec. IV.

II. METHODOLOGY

A. Color-gradient-based phase-field model

In the conventional two-phase CG method [19,32], two fluids are represented by the so-called *red* (subscript and superscript r) and *blue* (subscript and superscript b) fluids. The corresponding particle distribution functions (PDFs) $f_\alpha^r(\boldsymbol{x},t)$ and $f_\alpha^b(\boldsymbol{x},t)$ are introduced to represent them, and the local density of the fluid k (k denotes the fluid being either *red* or *blue*), i.e., $\tilde{\rho}_k$, is given by the first moments of the PDF, i.e., $\tilde{\rho}_k = \sum_\alpha f_\alpha^k(\boldsymbol{x},t)$ with $\boldsymbol{x}$ and t being the position and time, respectively. The total density is given by $\rho = \tilde{\rho}_r + \tilde{\rho}_b$. In most studies [28], the summation of the two PDFs, i.e., $f_\alpha^r + f_\alpha^b$, undergoes a collision operator to recover the hydrodynamic properties, while there are a few studies that employ a separate LBE to do so [35]. Also, in the conventional CG method, a recoloring step is employed to impose the surface tension force. To separate the two fluids, a segregation step is employed in the CG method which resembles the conservative AC equation [36], still with distinct differences. In the CG method, the density of each fluid is determined based on the first moment of the PDF, and the phase field is determined based on the density fields. Also, for modeling fluid flows with density contrast with the CG method, some manipulations need to be taken care of since the density field is coupled with the hydrodynamic properties such as pressure and sound speed [17,27,33]. On the other hand, in the context of the phase-field method for incompressible and immiscible fluids, the density field can be computed based on the value of the phase field. We take into account these differences when building our formulation of the CG method in this study.

By considering the segregation step, proposed by Latva-Kokko and Rothman [19] and treating the recoloring step in a CSF manner [18], the following macroscopic equations are recovered through the CE analysis expansion [28,35]:

$$\begin{aligned}
\frac{\partial \tilde{\rho}_r}{\partial t} + \nabla\cdot(\tilde{\rho}_r \boldsymbol{u}) &= D\nabla^2\tilde{\rho}_r - 2D\beta\nabla\cdot\left(\frac{\tilde{\rho}_r\tilde{\rho}_b}{\tilde{\rho}_r+\tilde{\rho}_b}\boldsymbol{n}\right),\\
\frac{\partial \tilde{\rho}_b}{\partial t} + \nabla\cdot(\tilde{\rho}_b \boldsymbol{u}) &= D\nabla^2\tilde{\rho}_b + 2D\beta\nabla\cdot\left(\frac{\tilde{\rho}_r\tilde{\rho}_b}{\tilde{\rho}_r+\tilde{\rho}_b}\boldsymbol{n}\right),
\end{aligned} \tag{1}$$

where $\boldsymbol{u}$ is the fluid velocity, $0<\beta<1$ is the segregation parameter that controls the interface thickness, and $\boldsymbol{n}$ is the unit vector normal to the interface. In the above equation D acts like mobility in the phase-field context and is related to the sound speed and the pressure field [27,33].

In the context of phase-field modeling, the phase field is defined as $N_k = \tilde{\rho}_k/\rho_k$, where ρ_k is the bulk density value of the fluid k. The phase field of a volume has its bulk values of unity (zero) if the volume is filled with (empty of) the corresponding fluid, and changes smoothly across the interfaces. By dividing Eq. (1) by the bulk density we reach the following equations

$$\begin{aligned}
\frac{\partial N_r}{\partial t} + \nabla\cdot(N_r \boldsymbol{u}) &= D\nabla^2 N_r - 2D\beta\nabla\cdot\left(\frac{N_r N_b}{N_r(\rho_r/\rho_b)+N_b}\boldsymbol{n}\right),\\
\frac{\partial N_b}{\partial t} + \nabla\cdot(N_b \boldsymbol{u}) &= D\nabla^2 N_b + 2D\beta\nabla\cdot\left(\frac{N_r N_b}{N_r+N_b(\rho_b/\rho_r)}\boldsymbol{n}\right),
\end{aligned} \tag{2}$$

in which we have assumed that there is no difference between the interface normal vector **n** if it is calculated based on the density field or phase field. As can be seen in Eq. (2) by defining the segregation factor as $\beta = 2/W$, with W being the interface thickness, and also treating D as a constant mobility as defined in the AC framework, we reach the same equation as the AC one provided that the density of the two fluids matches, i.e., $\rho_r = \rho_b$. The AC model strives to reach an equilibrium interface profile in the shape of a hyperbolic tangent with the concept of the equilibrium profile in the thermodynamically derived phase-field models [37]. From a symmetrical point of view, Eq. (2) is only valid when $\rho_r = \rho_b$, which means that Eq. (1) can only be used for density matched fluids, which explains why the CG original method faces difficulties in tackling density contrast fluids. As can be seen, for mixtures with density contrasts, the phase field computed in Eq. (2) no longer corresponds to the equilibrium profile of its corresponding AC equation, and careful treatments must be made such as defining D based on the density-based sound ratio [17,27]. Differences between Eqs. (1) and (2) are further discussed in Sec. III E.

In this paper, we propose to solve the following equation [setting $\rho_r = \rho_b$ in Eq. (2)] for the phase fields N_k, which are bounded within the range [0, 1], i.e.,

$$\begin{aligned}\frac{\partial N_r}{\partial t} + \boldsymbol{\nabla}\cdot(N_r\boldsymbol{u}) &= D\nabla^2 N_r - 2D\beta\boldsymbol{\nabla}\cdot\left(\frac{N_r N_b}{N_r+N_b}\boldsymbol{n}\right),\\ \frac{\partial N_b}{\partial t} + \boldsymbol{\nabla}\cdot(N_b\boldsymbol{u}) &= D\nabla^2 N_b + 2D\beta\boldsymbol{\nabla}\cdot\left(\frac{N_r N_b}{N_r+N_b}\boldsymbol{n}\right).\end{aligned} \tag{3}$$

The density field is determined through a linear interpolation of the bulk densities through

$$\rho = \tilde{\rho}_r + \tilde{\rho}_b = N_r\rho_r + N_b\rho_b. \tag{4}$$

To determine the location of the interface and the unit vector normal to the interface, the following auxiliary phase field is defined

$$\phi = \frac{1}{2}\left(\frac{N_r - N_b}{N_r + N_b} + 1\right) \tag{5}$$

with $\phi = 1$ indicating pure *red* fluid and $\phi = 0$ indicating pure *blue* fluid. The unit vector normal to the interface can be calculated by $\boldsymbol{n} = \boldsymbol{\nabla}\phi/|\boldsymbol{\nabla}\phi|$.

B. LBE for interface capturing

The following LBEs are employed to solve Eqs. (3):

$$f_\alpha^k(\boldsymbol{x} + \boldsymbol{e}_\alpha\delta t, t+\delta t) = f_\alpha^k(\boldsymbol{x},t) + \Omega_\alpha^{N,k}(\boldsymbol{x},t) + \delta t\left(\frac{2\tau^N - 1}{2\tau^N}\right)F_\alpha^{N,k}(\boldsymbol{x},t), \tag{6}$$

where $\boldsymbol{e}_\alpha$ gives the velocity in the α direction, Ω^N is the collision operator, F^N is a source term, and τ^N is the dimensionless relaxation time in the single-relaxation-time (SRT) collision operator. It should be noted that in some CG models the surface tension force is included in the interface-capturing equations [28]. In contrast, the proposed model does not consider the interfacial force; instead, it only takes effect in the hydrodynamic equation, as discussed in Sec. II C.

Equation (6) is different from commonly used CG equations. First, in the original CG method, i.e., Gunstensen *et al.* [11], the collision operator includes three terms, i.e., single-phase collision operator, perturbation step, and recoloring step. However, the present study only includes the term responsible for the relaxation of PDFs. Second, as we treat the surface tension in a CSF manner [18], and consider it only in the hydrodynamic equations, the collision operator does not include a forcing term. Finally, the recoloring step, which separates the two phases, is embedded in the interface-capturing equations. Therefore, the collision operator can be written as

$$\Omega_\alpha^{N,k} = -\frac{1}{\tau^N}\left(f_\alpha^k - f_\alpha^{k,\mathrm{eq}}\right) \tag{7}$$

and the source term in Eq. (6) is defined as

$$F_\alpha^{N,r} = -F_\alpha^{N,b} = 2\beta\frac{N_r N_b}{N_r+N_b}w_\alpha\boldsymbol{e}_\alpha\cdot\boldsymbol{n}. \tag{8}$$

In Eq. (7) $f_\alpha^{k,\mathrm{eq}}$ is the equilibrium distribution of f_α^k, which is defined as

$$f_\alpha^{k,\mathrm{eq}} = N_k w_\alpha\left(1 + \frac{\boldsymbol{e}_\alpha\cdot\boldsymbol{u}}{c_s^2} + \frac{(\boldsymbol{e}_\alpha\cdot\boldsymbol{u})^2}{2c_s^4} - \frac{\boldsymbol{u}\cdot\boldsymbol{u}}{2c_s^2}\right), \tag{9}$$

where $c_s = c/\sqrt{3}$ with $c = \delta x/\delta t$, and w_α is the weight coefficient. The phase fields of the two fluids are calculated based on the zeroth moment of the PDFs, i.e., $N_k = \sum_\alpha f_\alpha^k(\boldsymbol{x},t)$ for $k = r$ or b. Also, the mobility is related to the dimensionless relaxation time by

$$D = \tau^N c_s^2\delta t. \tag{10}$$

The lattice velocity and weight coefficient for a two-dimensional (2D) and a nine-velocity lattice (known as D2Q9) are given as

$$\boldsymbol{e}_\alpha = c\begin{cases}(0,0), & \alpha = 0,\\ (\cos[(\alpha-1)\pi/2], \sin[(\alpha-1)\pi/2]), & \alpha = 1,2,3,4,\\ (\cos[(2\alpha-9)\pi/4], \sin[(2\alpha-9)\pi/4])\sqrt{2}, & \alpha = 5,6,7,8,\end{cases} \tag{11}$$

$$w_\alpha = \begin{cases}4/9, & \alpha = 0,\\ 1/9, & \alpha = 1,2,3,4,\\ 1/36, & \alpha = 5,6,7,8.\end{cases} \tag{12}$$

C. LBE for hydrodynamics

To recover the hydrodynamic equations (see Appendix B), we can implement either velocity-based or momentum-based formulations. The former, which is the method of choice in this study, has less incompressibility error compared to the latter and has already been employed by several researchers due to its improved numerical stability and accuracy [34,38–40]. Here, we employ a velocity-based LB model originally proposed by Zu and He [38] and recently improved by Fakhari *et al.* [34]. The following LBE for the hydrodynamic equations is used [34]:

$$g_\alpha(\boldsymbol{x}+\boldsymbol{e}_\alpha\delta t, t+\delta t) = g_\alpha(\boldsymbol{x},t) + \Omega_\alpha(\boldsymbol{x},t) + F_\alpha(\boldsymbol{x},t), \quad (13)$$

where g_α is the hydrodynamic distribution function, Ω_α is the collision operator [Eqs. (14) and (15)], and F_α is the source term [Eq. (21)].

The generalized collision operator can be written as either a SRT collision operator [34],

$$\Omega_\alpha^{\mathrm{SRT}} = -\frac{1}{\tau+1/2}\left(g_\alpha - \bar{g}_\alpha^{\mathrm{eq}}\right), \quad (14)$$

or as a multiple-relaxation-time (MRT) collision operator [34],

$$\Omega_\alpha^{\mathrm{MRT}} = \mathbf{M}^{-1}\hat{\mathbf{S}}\mathbf{M}\left(g_\alpha - \bar{g}_\alpha^{\mathrm{eq}}\right), \quad (15)$$

where $\bar{g}_\alpha^{\mathrm{eq}}$ is the modified equilibrium distribution function defined as

$$\bar{g}_\alpha^{\mathrm{eq}} = g_\alpha^{\mathrm{eq}} - \tfrac{1}{2}F_\alpha, \quad (16)$$

where

$$g_\alpha^{\mathrm{eq}} = \frac{p}{\rho c_s^2}w_\alpha + \Gamma_\alpha - w_\alpha, \quad (17)$$

where p is the macroscopic pressure. In the MRT collision operator, $\mathbf{M}$ and $\mathbf{M}^{-1}$ are the orthogonal transformation matrix and its inverse, respectively, and $\hat{\mathbf{S}}$ is the diagonal relaxation matrix [41], which takes the following form in this study [34]:

$$\hat{\mathbf{S}} = \mathrm{diag}\left(1,1,1,1,1,1,1,\frac{1}{\tau+1/2},\frac{1}{\tau+1/2}\right) \quad (18)$$

It should be noted that, in this study, only the MRT model is employed. The hydrodynamic relaxation time τ is related to the kinematic viscosity of the fluid ν by

$$\tau = \frac{\nu}{c_s^2\delta t}. \quad (19)$$

The relaxation time across the interface can be given by different interpolation schemes [34]. Similarly to the density field, a linear interpolation is used for the relaxation time in this study:

$$\tau = N_r\tau_r + N_b\tau_b. \quad (20)$$

The source term in Eq. (13) is given by

$$F_\alpha = \delta t\, w_\alpha \frac{\boldsymbol{e}_\alpha\cdot\boldsymbol{F}}{\rho c_s^2}, \quad (21)$$

where the force $\boldsymbol{F}$ includes four different terms [34]:

$$\boldsymbol{F} = \boldsymbol{F}_g + \boldsymbol{F}_a + \boldsymbol{F}_p + \boldsymbol{F}_\eta + \boldsymbol{F}_s, \quad (22)$$

where $\boldsymbol{F}_g = \rho\boldsymbol{g}$ is the body force with $\boldsymbol{g}$ being the gravitational acceleration. An additional term appears in the hydrodynamic equations if a phase-field model is employed for capturing the interfaces [42]. For the present model, it has the following shape:

$$\begin{aligned}\boldsymbol{F}_a &= -\boldsymbol{u}\left(\frac{d\rho}{dN_r}\frac{dN_r}{dt} + \frac{d\rho}{dN_b}\frac{dN_b}{dt}\right)\\ &= -\boldsymbol{u}D\Big[\rho_r\nabla^2N_r + \rho_b\nabla^2N_b - 2\beta(\rho_r-\rho_b)\\ &\quad\times\nabla\cdot\left(\frac{N_rN_b}{N_r+N_b}\boldsymbol{n}\right)\Big]\end{aligned} \quad (23)$$

with d being the derivative operator.

Two additional force terms, namely the *pressure correction term*, $\boldsymbol{F}_p$, and the *viscous stress correction term*, $\boldsymbol{F}_\eta$, are included in the force term to exactly recover the Navier-Stokes equations (NSs) [34]. These two terms are given by

$$\boldsymbol{F}_p = -\frac{p}{\rho}\nabla\rho \quad (24)$$

and

$$\boldsymbol{F}_\eta = \nu[\nabla\boldsymbol{u} + (\nabla\boldsymbol{u})^T]\cdot\nabla\rho. \quad (25)$$

One can use finite differences to calculate $\boldsymbol{F}_\eta$ based on Eq. (25). In this study, we calculate $\boldsymbol{F}_\eta$ based on the central moments as proposed by Fakhari *et al.* [34]. For the SRT model we have

$$F_{\eta,n}^{\mathrm{BGK}} = -\frac{\nu}{(\tau+1/2)c_s^2\delta t}\left[\sum_\alpha e_{\alpha n}e_{\alpha m}\left(g_\alpha - g_\alpha^{\mathrm{eq}}\right)\right]\frac{\partial\rho}{\partial x_m}, \quad \{m,n\}\in\{x,y\}, \quad (26)$$

and for the MRT one we have

$$F_{\eta,n}^{\mathrm{MRT}} = -\frac{\nu}{c_s^2\delta t}\left[\sum_\beta e_{\beta n}e_{\beta m}\sum_\alpha(\mathbf{M}^{-1}\hat{\mathbf{S}}\mathbf{M})_{\beta\alpha}\left(g_\alpha - g_\alpha^{\mathrm{eq}}\right)\right]\frac{\partial\rho}{\partial x_m}, \quad \{m,n\}\in\{x,y\}, \quad (27)$$

where the subscripts α and β denote the characteristic directions.

In most CG models, the interfacial force is defined based on the CSF with the following definition [43]:

$$\boldsymbol{F}_s = -\sigma\kappa\nabla\phi, \quad (28)$$

where σ is interfacial tension and κ is the curvature, which is defined as

$$\kappa = -[\boldsymbol{I} - \boldsymbol{n} \otimes \boldsymbol{n} \cdot \nabla] \cdot \boldsymbol{n}. \tag{29}$$

However, this interfacial force includes the derivative of the unit normal vector and may induce undesirable discretization errors. We will therefore employ a chemical-potential-based interfacial force defined as [44]

$$\boldsymbol{F}_s = \mu \nabla \phi, \tag{30}$$

where μ is the chemical potential defined by

$$\mu = 12\sigma\beta\phi(1-\phi)(1-2\phi) - \frac{3\sigma}{\beta}\nabla^2\phi. \tag{31}$$

After the streaming step, the hydrodynamic properties are calculated by taking the zeroth and first moments of the hydrodynamic distribution function according to

$$p = \rho c_s^2 \sum_\alpha g_\alpha, \tag{32}$$

$$\boldsymbol{u} = \sum_\alpha \boldsymbol{e}_\alpha g_\alpha + \frac{\boldsymbol{F}}{2\rho}\delta t. \tag{33}$$

In the above equations, the partial derivatives are calculated using the following scheme:

$$\nabla\lambda(\boldsymbol{x}, t) = \frac{c}{c_s^2 \delta x} \sum_\alpha \boldsymbol{e}_\alpha w_\alpha \lambda(\boldsymbol{x} + \boldsymbol{e}_\alpha \delta t, t), \tag{34}$$

where λ is a placeholder for any quantity.

III. RESULTS

To assess the accuracy and stability of the proposed model, different benchmark tests are conducted. Two LB models are considered. The first is the model of Fakhari *et al.* [34] in which the AC equation is solved (called the AC model). The second model is a commonly used CG model by Akai *et al.* [28] (called the CG model).

In the first four tests, we only consider the interface-evolution equations alone, and so the velocity field is prescribed. The results are compared with analytical solutions as well as the AC model. Note that the mobility in the proposed model is not related to the hydrodynamic properties but rather a constant parameter determined by Eq. (10) based on the accuracy and stability of the model [45]. In the rest of the tests, the hydrodynamic equations are also solved and they are coupled with the interface-evolution equations through the phase fields and velocity field. Throughout the paper, the interface is fixed where the auxiliary phase field is $\phi = 0.5$.

To consistently compare the results with other available data, we use the Péclet number $\mathrm{Pe} = L_0 U_0 / D$ and the Cahn number $\mathrm{Ch} = W/L_0$, where U_0 and L_0 are the reference velocity and reference length, respectively. Also, we define the density and viscosity ratios as $\rho^* = \rho_r/\rho_b$ and $\eta^* = \eta_r/\eta_b$, respectively, with $\eta = \rho\nu$ being the dynamic viscosity. In what follows, the dimensionless time is defined as $t^* = t/t_0$, where t is the number of iterations and t_0 is the reference time that is defined in each test case. Also, the *red* and *blue* fluids are considered to be the heavy and light fluids, respectively.

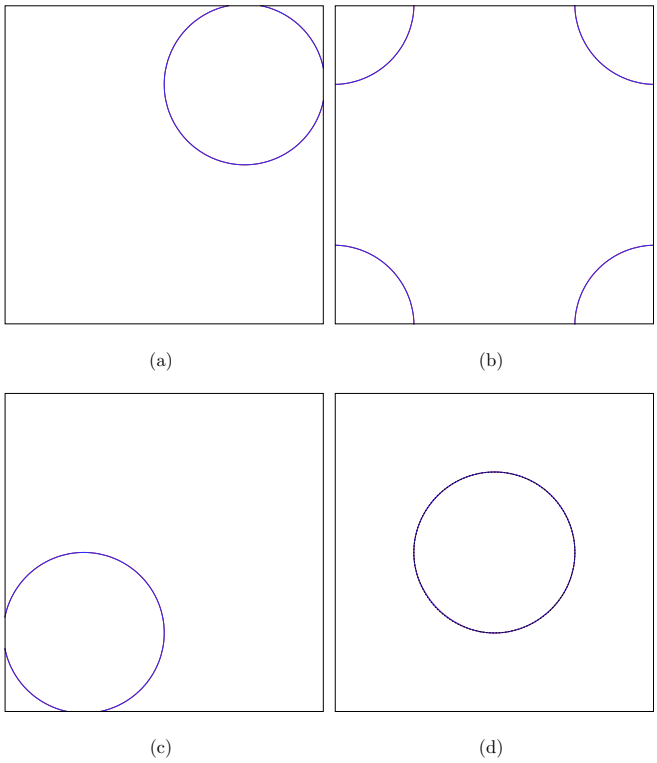

FIG. 1. Diagonal translation of a circular interface at $\mathrm{Pe} = 62.5$ and $\mathrm{Ch} = 3/100$. (a) $t^* = 0.25$, (b) $t^* = 0.50$, (c) $t^* = 0.75$, (d) $t^* = 10.0$. The analytical profile is shown by a black dashed line at $t^* = 10.0$; however, it is covered by the result of the introduced model (shown by the solid blue line) and the LB model [34] (shown by the red solid line).

A. Diagonal translation of circular interface

The diagonal translation of circular interface [46] is the first benchmark to verify the interface-capturing equations together with their LB solvers. A circular interface with an initial radius of $R = L_0/4$ is placed in the middle of a square domain with length $L_0 = 100$, and the following velocity field is prescribed:

$$\begin{aligned} u_x(x, y) &= U_0, \\ u_y(x, y) &= U_0. \end{aligned} \tag{35}$$

Unless otherwise specified, the inside of the interface is filled with the *red* fluid ($\phi = 1$), while the rest of the domain is filled with the *blue* fluid ($\phi = 0$). Also, the periodic boundary condition is applied for all sides, and the circular interface returns to its original configuration at $t^* = 1.0$ with the reference time defined as $t_0 = L_0/U_0$. Figure 1 shows the interface at different dimensionless times for $\mathrm{Pe} = 62.5$ and $\mathrm{Ch} = 3/100$. At $t^* = 10$, the analytical interface (the dashed line) is covered by the present simulation result (the solid blue line) and the AC model (the solid red line) indicating that the proposed model generates accurate results. There is almost no difference between the two LB models. To quantitatively assess the model and find the convergence rate, we define the following relative error:

$$\|\delta\phi\|_1 = \frac{\sum |\phi(\boldsymbol{x}, t) - \phi(\boldsymbol{x}, 0)|}{\sum_{\boldsymbol{x}} |\phi(\boldsymbol{x}, 0)|}, \tag{36}$$

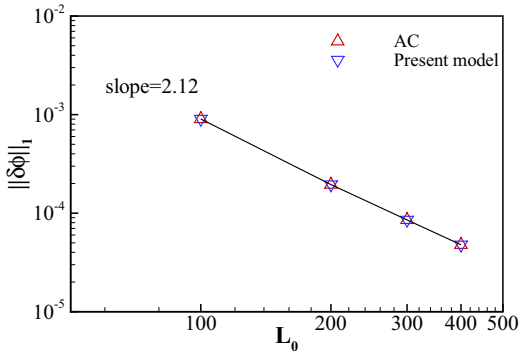

FIG. 2. Convergence rate of the relative error $\|\delta\phi\|_1$ versus different grid resolutions represented by the grid cell number L_0 for the diagonal translation of a circular interface (Pe = 62.5 and Ch = 3/100) for the present model and the AC model.

where $\phi(\boldsymbol{x}, t)$ is the computational phase field at time t and $\phi(\boldsymbol{x}, 0)$ is the initial phase field. Figure 2 shows the convergence rate by performing the test on four different grid resolutions with the same parameter as Fig. 1 at $t^* = 1$. As can be seen, the present model produces results with low error and with a convergence rate close to the second order, similar to the AC model.

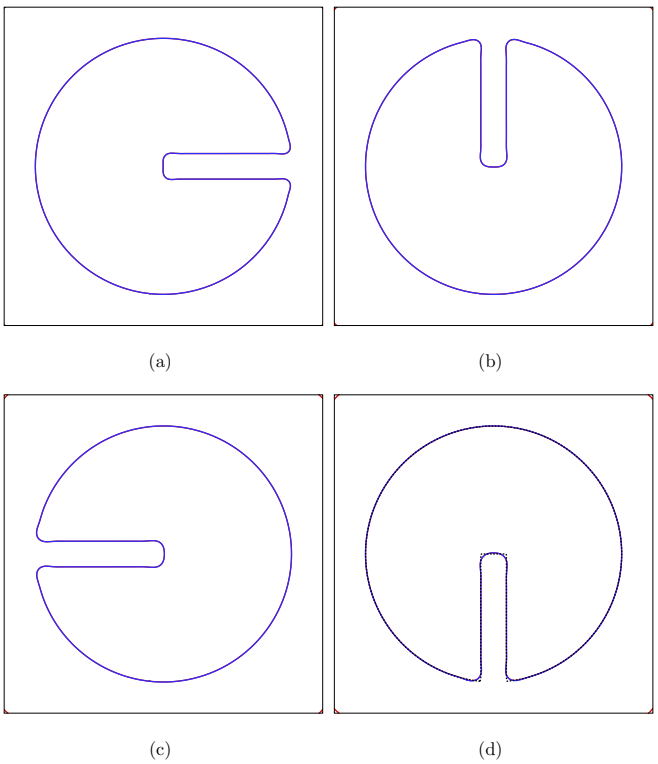

FIG. 3. Rotation of the Zalesak's disk at Pe = 500 and Ch = 3/200. (a) $t^* = 0.5$, (b) $t^* = 1.0$, (c) $t^* = 1.5$, (d) $t^* = 2.0$. The analytical profile is shown by the black dashed line at $t^* = 2.0$ and is covered by the present result (shown by the solid blue line) and the AC model (shown by the red solid line). Note the red lines in the corners, indicating unphysical behavior for the AC model.

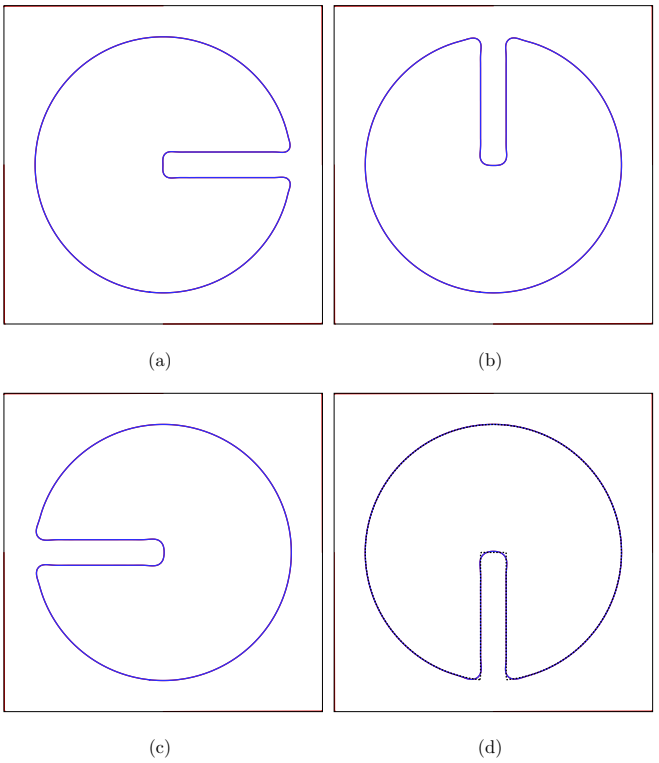

FIG. 4. Rotation of the Zalesak's disk with the zero-gradient boundary condition. The parameters are the same as in Fig. 3. (a) $t^* = 0.5$, (b) $t^* = 1.0$, (c) $t^* = 1.5$, (d) $t^* = 2.0$. The analytical profile is shown by the black dashed line at $t^* = 2.0$ and is covered by the present result (shown by the solid blue line) and the AC model (shown by the red solid line). Note the red lines at the boundaries, indicating unphysical behavior for the AC model, similar to what was observed in Fig. 3.

B. Rotation of Zalesak's disk

The Zalesak's disk [47] rotation is another benchmark test that has been widely used to evaluate interface-capturing equations [38,46]. A disk with the initial radius of $R = 2L_0/5$ and slot width of $3L_0/40$ is placed at the center of a square domain with the length $L_0 = 200$. The periodic boundary condition is considered for this test as used in different studies, e.g., Geier *et al.* [46] and Zu and He [38]. The disk is driven by a vortex flow with the velocity field as

$$u_x(x, y) = -U_0\pi\left(\frac{y}{L_0} - 0.5\right),$$
$$u_y(x, y) = U_0\pi\left(\frac{x}{L_0} - 0.5\right). \tag{37}$$

The disk rotates back to its original configuration at $t^* = 2$ with $t_0 = L_0/U_0$. Figure 3 shows the disk at different dimensionless times for Pe = 500 and Ch = 3/200. As can be seen, the slotted disk maintains its initial shape during the rotation. As can be seen, the AC model results in unphysical disturbances around the four corners of the computational domain. As suggested by Fakhari *et al.* [48], a zero-gradient boundary condition for all boundaries is applied. The results are shown in Fig. 4. As can be seen, boundary errors exist for the AC

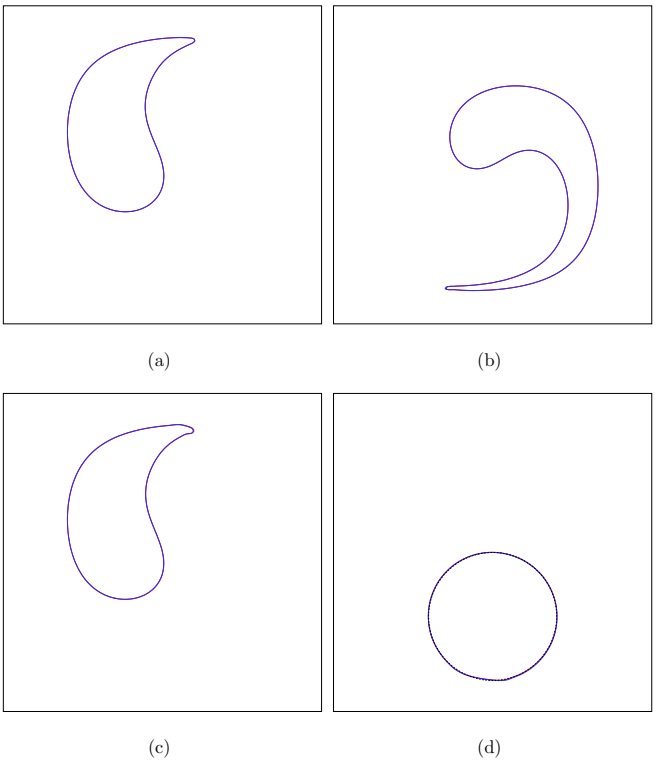

FIG. 5. A circular interface in a shear flow at Pe = 500 and Ch = 3/100. (a) $t^* = 0.5$, (b) $t^* = 1.0$, (c) $t^* = 1.5$, (d) $t^* = 2.0$. The analytical profile is shown by the black dashed line at $t^* = 2.0$ and is covered by the present result (shown by the solid blue line) and the AC model (shown by the red solid line).

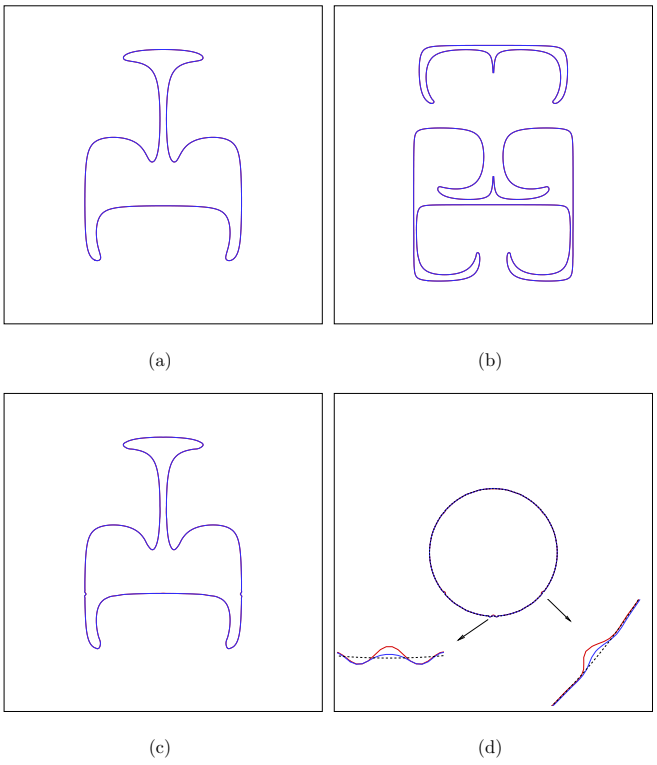

FIG. 6. Deformation of a circular interface at Pe = 1250 and Ch = 3/500. (a) $t^* = 0.25$, (b) $t^* = 0.5$, (c) $t^* = 0.75$, (d) $t^* = 1.0$. The analytical profile is shown by the black dashed line at $t^* = 1$ and is covered by the present result (shown by the solid blue line) and the AC model (shown by the red solid line).

model, thus the present model gives slightly better interface capturing.

C. Circular interface in a shear flow

For the third benchmark problem, we place a circular interface of radius $R = L_0/5$ in a square domain with $L_0 = 200$. The center of the circular interface is located at $(L_0/2, 3L_0/10)$. The periodic boundary condition is considered for all sides. The following shear flow is prescribed:

$$\begin{aligned} u_x(x,y) &= -U_0\pi \cos\left[\pi\left(\frac{x}{L_0} - 0.5\right)\right] \\ &\quad \times \sin\left[\pi\left(\frac{y}{L_0} - 0.5\right)\right], \\ u_y(x,y) &= U_0\pi \sin\left[\pi\left(\frac{x}{L_0} - 0.5\right)\right] \\ &\quad \times \cos\left[\pi\left(\frac{y}{L_0} - 0.5\right)\right]. \end{aligned} \tag{38}$$

The velocity field is reversed at $t^* = 1$ so that the circular interface comes back to its original position at $t^* = 2$. The reference time is defined as $t_0 = L_0/U_0$. The other parameters are Pe = 500 and Ch = 3/200. Figure 5 shows the interface pattern at different times. As can be seen, for this benchmark, there is little difference between the present model and the AC model.

D. Deformation of a circular interface

Another test considered is the deformation of a circular interface, which is considered a particularly stringent problem [49]. The following velocity field causes large topological changes, thus posing challenges for interface-evolution equations

$$\begin{aligned} u_x(x,y) &= -U_0 \sin\left[4\pi\left(\frac{x}{L_0} + 0.5\right)\right] \\ &\quad \times \sin\left[4\pi\left(\frac{y}{L_0} + 0.5\right)\right], \\ u_y(x,y) &= -U_0 \cos\left[4\pi\left(\frac{x}{L_0} + 0.5\right)\right] \\ &\quad \times \cos\left[4\pi\left(\frac{y}{L_0} + 0.5\right)\right], \end{aligned} \tag{39}$$

where the velocity is abruptly reversed at $t^* = 0.5$ and the interface returns to its initial position at $t^* = 1$ ($t_0 = L_0/U_0$). A periodic square domain with the length of $L_0 = 500$ is considered and a circular interface with a radius of $R = L_0/5$ is placed at the center of the domain. Other parameters are Pe = 1250 and Ch = 3/500. Figure 6 shows the interface at different times. As can be seen, there is disintegration and reconsolidation of the interface, which is caused by the abrupt change in the velocity as well as a sharp initial velocity. Also, there are some discrepancies between the initial and final

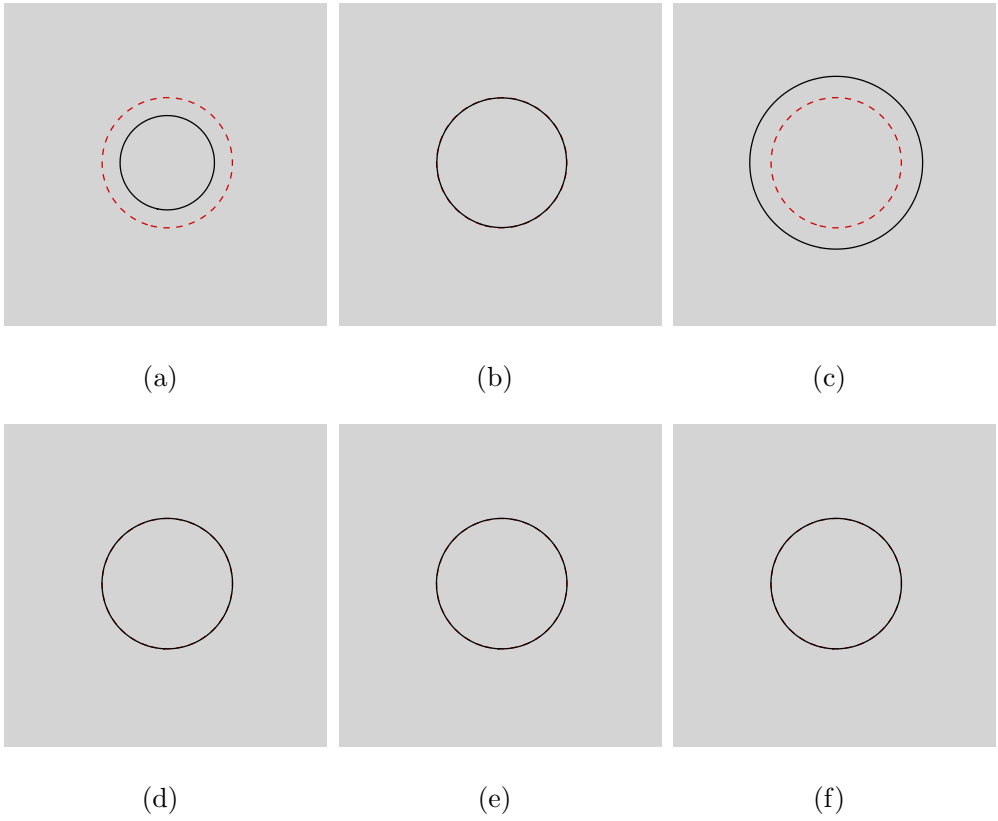

FIG. 7. Circular droplet in a periodic domain for different density ratios of (a) $\rho^* = 0.5$, (b) $\rho^* = 1.0$, (c) $\rho^* = 2.0$ for the original CG model [Eq. (1)] and (d) $\rho^* = 0.5$, (e) $\rho^* = 1.0$, (f) $\rho^* = 2.0$ for the present model (Eq. (3)). Solid black lines show the interface profiles at the steady-state condition while the red dashed lines represent the initial interface.

shapes as shown at $t^* = 1$. As can be seen, the present model performs slightly better than the AC model. It should be noted that this improvement comes at an increase in computational cost. As shown in Sec. II, the CG method resembles the AC phase-field equation. However, the CG results in more accurate results at the cost of computational resources. As such, there is a compromise to be made between accuracy and computational cost.

E. Laplace test

In the following tests, the hydrodynamic equations [Eq. (13)] for determining the velocity and pressure field are also solved. We first point out the differences between the density capturing equation (1) (which is the CG model [28]) and interface-capturing equation (3) (which is the present model). A droplet with a radius of $R = L_0/5$ is placed at the center of a 2D domain with a side length of $L_0 = 100$. All four sides are treated as periodic boundary conditions. Other parameters are $W = 2.85$, $D = 1/6$, and $\sigma = 0.001$. Figure 7 shows the results of the two methods for three different density ratios, namely $\rho^* = 0.5$, $\rho^* = 1.0$, and $\rho^* = 2.0$ ($\rho_r = 1$). In all cases, $\eta^* = 1$ ($\eta_r = 0.5/3$). The initial interface is shown by a dashed line while the steady-state interface is shown by a solid line. This figure supports the conclusion that the original CG model is not well adapted to mixtures with density contrasts, and to make it applicable some treatments need to be employed [27,33]. For the case of $\rho^* = 0.5$ the droplet shrinks, while for the case of $\rho^* = 2.0$ it expands until its density reaches the density of unity. However, in the present model, the volume of the droplet does not change, and it shows a good interface-capturing ability. It should be noted that in both methods the mass is conserved accurately. Due to this droplet shrinkage or expansion for the original CG model, the rest of the section only includes the results of the present model.

The parasitic currents (or spurious velocities) are small amplitude velocities around the interfaces and are caused by errors in the computation of the interfacial forces. We consider a high density and viscosity contrast mixture with the properties of $\rho^* = 1000$ ($\rho_r = 1$), $\eta^* = 100$ ($\eta_r = 0.05/3$). Other parameters are the same as before. Two different cases with interfacial tension $\sigma = 0.001$ and $\sigma = 0$ are investigated. The parasitic velocities and the maximum of the kinetic energy, $\mathrm{KE} = \rho|\boldsymbol{u}|^2/2$, are shown in Figs. 8 and 9, respectively. As can be seen for $\sigma \neq 0$, around the droplets there exist parasitic currents which are attributed to different causes [50], and are caused to vanish by the viscous force, as Fig. 9 suggests. These parasitic currents vanish in case of zero surface tension for the present model, in contrast to CG models [27,28] in which the surface tension force is included in the interface-capturing equation and the mobility is related to the density and pressure fields with no distinct equations for solving the hydrodynamic properties.

To further investigate the accuracy of the model in handling fluid flows with high density and viscosity contrasts, the

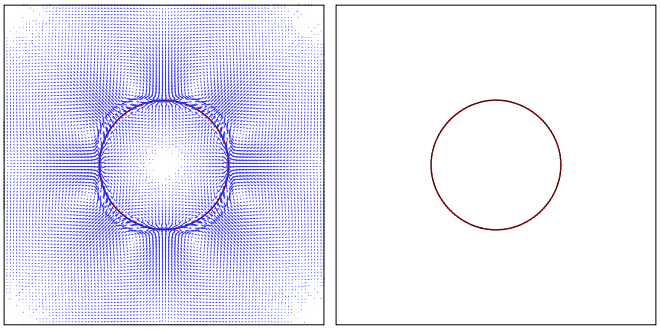

(a) (b)

FIG. 8. Parasitic currents for a static droplet in a quiescent surrounding fluid (a) $\sigma = 0.001$ and (b) $\sigma = 0$. The velocity vectors are shown in blue color and scaled by 2×10^5 in lattice units. Solid black lines represent the interface at the steady state while the red dashed lines correspond to the initial interface.

phase field profile along the horizontal centerline ($y = L_0/2$) is shown in Fig. 10. As can be seen, the model results in a thin interface, and the interface profile for the two different surface tensions is the same as the initial one, which confirms the accuracy of the model. The Laplace law for different radii is also investigated. According to this law, the pressure difference across a 2D interface with radius R is related to the surface tension via

$$\Delta p = \frac{\sigma}{R}. \tag{40}$$

Figure 11 shows the Laplace law for different radii when $\sigma = 0.001$, and is in good agreement with the analytical relation (40).

F. Rayleigh-Taylor instability

The Rayleigh-Taylor instability (RTI) has been used as a benchmark in validating multiphase models. A layer of heavy fluid lies above a lighter fluid in a gravitational field. A strong enough perturbation at the interface results in the replacement of the two fluids. A 2D domain of size $L_0 \times 4L_0$ with $L_0 = 256$ is selected. The upper and bottom boundaries

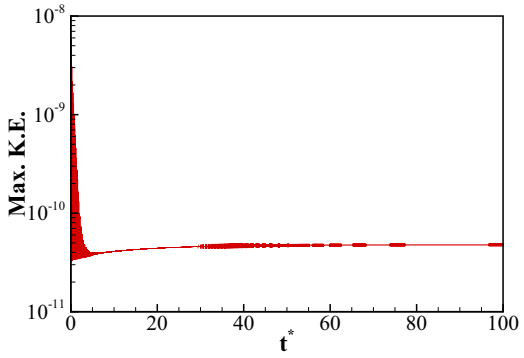

FIG. 9. Maximum kinetic energy versus dimensionless time for the case with interfacial tension $\sigma = 0.001$. Note that for $\sigma = 0$ the model results in the zero velocity field. The reference time is defined as $t_0 = \eta_r R/\sigma$.

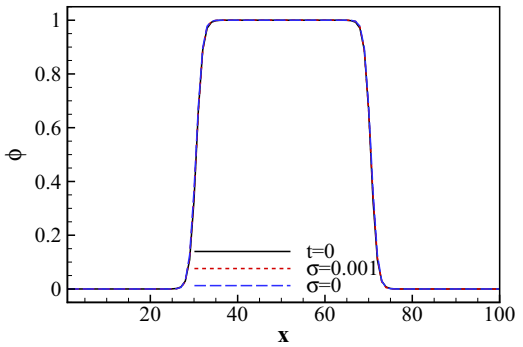

FIG. 10. Phase field profile along the horizontal centerline.

are treated as no-slip, while the vertical boundaries are considered as periodic. The phase field is initialized as

$$\phi = 0.5 + 0.5 \tanh\left[\frac{2(y - y_c - y_p)}{W}\right] \tag{41}$$

where $y_p = 0.1L_0 \cos(2\pi x/L_0)$ is a cosinusoidal perturbation to the interface, $y_c = 2L_0$ is the height of the unperturbed interface, and W is the interface thickness as defined before. Note that the left bottom corner is considered as the origin of the coordinates.

To compare the results of the present model with others, we consider several dimensionless numbers: The Reynolds (Re) and Atwood (At) numbers are defined as

$$\mathrm{Re} = \frac{\rho_r U_0 L_0}{\eta_r}, \tag{42}$$

$$\mathrm{At} = \frac{\rho_r - \rho_b}{\rho_r + \rho_b}. \tag{43}$$

The capillary number, which combines the inertial, viscous, and capillary forces, is defined as

$$\mathrm{Ca} = \frac{\eta_r U_0}{\sigma}. \tag{44}$$

In the above dimensionless numbers, $U_0 = \sqrt{gL_0}$ is the reference velocity. The phase field at different dimensionless times with $t_0 = \sqrt{L_0/g\mathrm{At}}$ are shown in Fig. 12 for $\mathrm{Re} = 3000$, $\mathrm{At} = 0.5$, $\mathrm{Ca} = 0.26$, $\rho^* = 3$, $\eta^* = 1$, $\mathrm{Pe} = 0.68$, and $\mathrm{Ch} = 5/256$. The results shown are in agreement with the available data [34], which confirms the accuracy of the model.

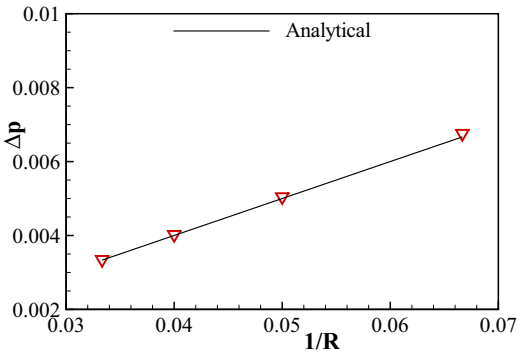

FIG. 11. Laplace law verification.

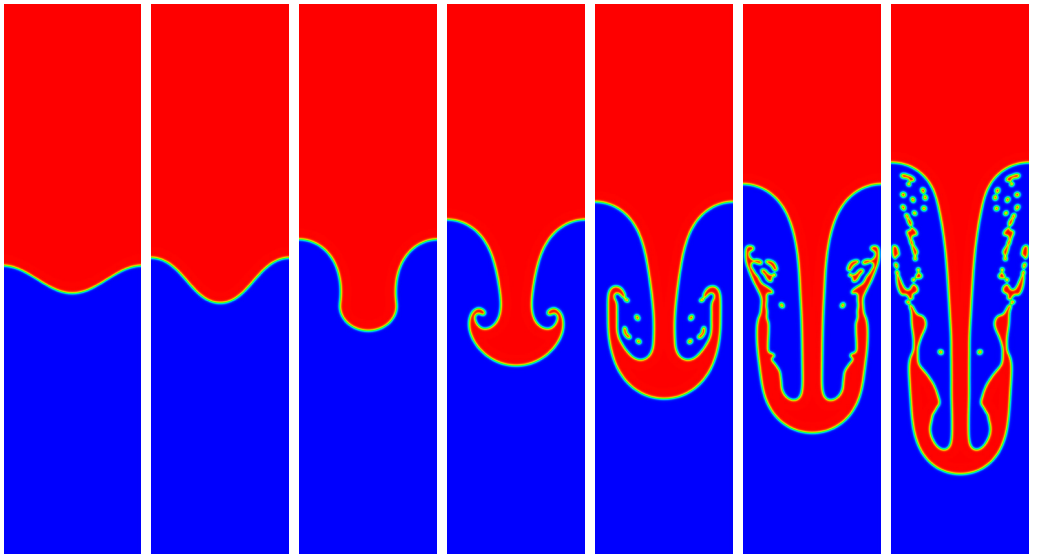

(a) $t^* = 0$ (b) $t^* = 0.5$ (c) $t^* = 1.0$ (d) $t^* = 1.5$ (e) $t^* = 2.0$ (f) $t^* = 2.5$ (g) $t^* = 3.0$

FIG. 12. Time evolution of the RTI for $\rho^* = 3$ (At $= 0.5$), $\eta^* = 1$, Re $= 3000$, Pe $= 0.68$, Ch $= 5/256$, and Ca $= 0.26$.

The dimensionless front positions of the bubble (the lighter fluid) and liquid (the heavier fluid) are shown in Fig. 13, together with the results of other studies [34,38,51,52]. As can be seen, there is good agreement between the present results and available data.

Simulation of RTI for multiphase fluid flow with a high-density ratio and high Reynolds number is quite challenging, and few studies have succeeded in doing so [34,52,53]. To probe the applicability of the proposed model, a RTI system with $\rho^* = 1000$ (At $= 0.998$), $\eta^* = 100$, Re $= 3000$, Ca $= 0.87$ Pe $= 81.92$, and Ch $= 5/128$ is simulated. The snapshots of the phase field at a different dimensionless time are shown in Fig. 14. As can be seen, in contrast to the previous RTI modeling, no vortices are generated around the falling liquid, and the present model can handle multiphase fluid flows with the same density and viscosity contrasts as water-air systems.

G. Droplet splashing on a thin liquid film

A droplet splashing on a liquid film is common in nature, e.g., raindrops splashing on the ground, and in the industry, e.g., inkjet printing, fuel in internal engines, etc., and has been numerically studied by a number of researchers [53–55]. Figure 15(a) shows the schematic of the problem. A droplet with the radius of R is placed at (x_c, y_c) in contact with a film layer of thickness h in a computational domain of size $4L_0 \times L_0$. The film layer has the same properties as the droplet. The upper and bottom boundaries are no-slip, while the vertical ones are periodic. The system is usually characterized by the Reynolds number (Re) and the Weber number (We):

$$\mathrm{Re} = \frac{2\rho_r U_0 R}{\eta_r}, \tag{45}$$

$$\mathrm{We} = \frac{2\rho_r U_0^2 R}{\sigma}. \tag{46}$$

where U_0 is the initial droplet velocity. The reference time is $t_0 = 2R/U_0$. Figure 15 shows the phase field for different dimensionless time for Re $= 500$, We $= 8000$, $\rho^* = 1000$, $\eta^* = 40$, and $h^* = h/2R = 0.15$. Other numerical parameters are $L_0 = 500$, $(x_c, y_c) = (250, 130)$, Ch $= 5/500$, Pe $= 0.36$, and $U_0 = 0.005$. Included in the figure are the results of Shao and Shu [53] and Lee and Lin [54]. To the best of our

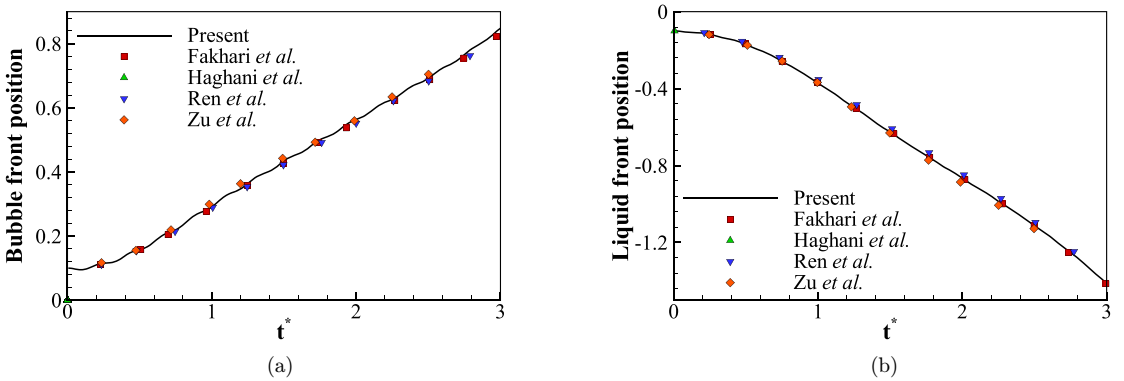

FIG. 13. Time evolution of (a) the bubble front position and (b) the liquid front position.

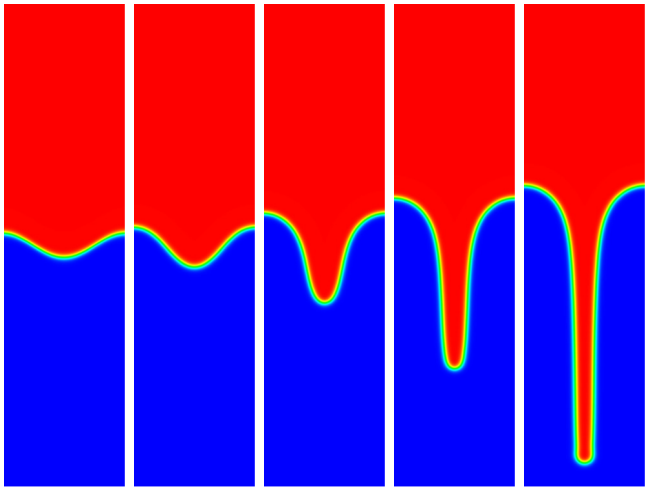

(a) $t^* = 0$ (b) $t^* = 0.5$ (c) $t^* = 1.0$ (d) $t^* = 1.5$ (e) $t^* = 2.0$

FIG. 14. Time evolution of the RTI for $\rho^* = 1000$ (At $= 0.998$), $\eta^* = 100$, Re $= 3000$, Pe $= 81.92$, Ch $= 5/128$, and Ca $= 0.87$.

knowledge, such an unsteady flow with a high-density ratio of 1000 considered in this benchmark has not been satisfactorily simulated in available CG models.

As can be seen in Fig. 15, after the droplet impacts the film, part of the lighter fluid is entrapped between the droplet

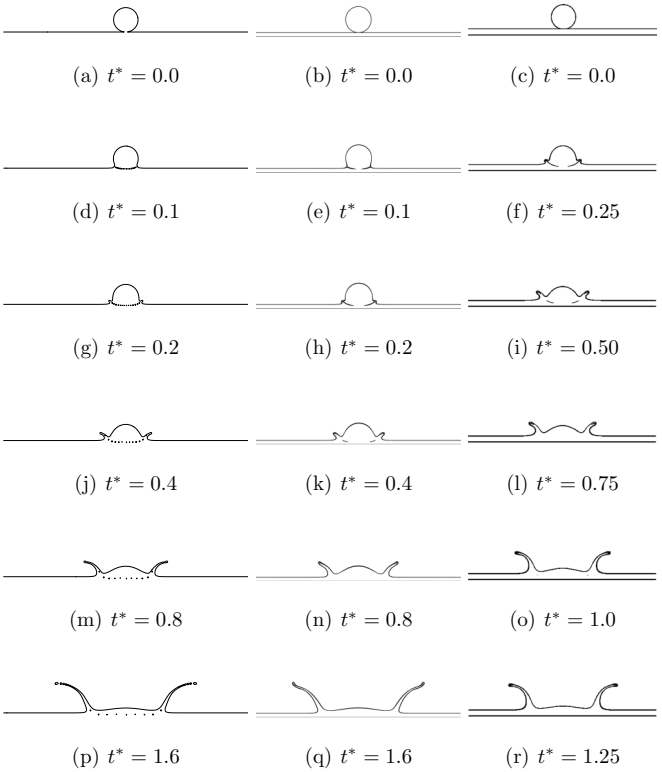

(a) $t^* = 0.0$ (b) $t^* = 0.0$ (c) $t^* = 0.0$

(d) $t^* = 0.1$ (e) $t^* = 0.1$ (f) $t^* = 0.25$

(g) $t^* = 0.2$ (h) $t^* = 0.2$ (i) $t^* = 0.50$

(j) $t^* = 0.4$ (k) $t^* = 0.4$ (l) $t^* = 0.75$

(m) $t^* = 0.8$ (n) $t^* = 0.8$ (o) $t^* = 1.0$

(p) $t^* = 1.6$ (q) $t^* = 1.6$ (r) $t^* = 1.25$

FIG. 15. Time evolution of the droplet splashing on a thin liquid film. The left frames are the results of the present model, the middle frames are the ones by Lee and Lin [54], and the right frames are the results of Shao and Shu [53].

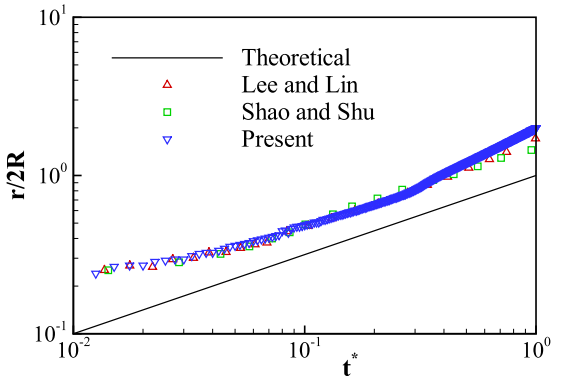

FIG. 16. Log-log plot of the spread factor $r/2R$ as a function of dimensionless time t^*. The straight line corresponds to the power law $r\sqrt{t}$.

and the film, and its shape changes from a thin film to small bubbles due to the surface tension. This phenomenon is correctly captured with the present model. However, these small bubbles will diffuse into the heavier fluid and eventually disappear in the other models. At later times, e.g., $t^* = 0.8$, 1.6 of the present results, the fingers of the heavy fluid become unstable and eventually break into smaller droplets due to the Rayleigh-Plateau instability (RPI). This instability is not observed in the results of the other two models.

Based on the potential flow solution, the spreading radius at early times is theoretically given by $r = \sqrt{2RU_0t}$ [55]. In the numerical simulation, the spreading radius is the position where the liquid velocity is at its maximum. Figure 16 compares the numerical spreading radius with the analytical solution and numerical results using the models from Refs. [53,54].

As can be seen, there is a good agreement between the present results and the other available data, which again confirms the accuracy and capability of the present model in high density and viscosity ratios. It should be noted that the discrepancy at the beginning of the impact in Fig. 16 is due to the impulsive collisions in numerical simulations which do not exist in the experiments [54].

IV. CONCLUSION

In this paper, the underlying difficulties of the color-gradient method in handling density-contrast mixture were explored. It was shown that the fluid invariant property of the CG hinders it from handling density-contrast mixtures, and a remedy based on the phase-field methodology was proposed. A formulation of the CG method was developed which is capable of handling high density and viscosity ratios in high Reynolds numbers without instability issues. This was achieved by treating the CG method as an interface-capturing method, and the lattice Boltzmann equations were developed to solve the macroscopic equations. At first, the interface-capturing equations were investigated by several benchmark tests to validate the accuracy and applicability of the proposed model. Then, the hydrodynamic equation was also taken into account, and challenging benchmark tests such as the Rayleigh-Taylor instability and a droplet splashing on a thin liquid film were conducted. The results were shown

to be in good agreement with the available data. Although the LB model was presented in 2D, its extension to 3D is straightforward and will be considered in future work.

ACKNOWLEDGMENTS

This work is financially supported by the Research Council of Norway, Projects No. 301412 and No. 262644 (PoreLab).

APPENDIX A

The CE analysis is conducted in this Appendix to derive the macroscopic interface-capturing Eq. (3) from the LBE (6). The constraints on $f_\alpha^{k,\mathrm{eq}}$ and $F_\alpha^{\phi,k}$ are as follows:

$$\begin{aligned}
\sum_\alpha f_\alpha^{k,\mathrm{eq}} &= N_k,\\
\sum_\alpha \boldsymbol{e}_\alpha f_\alpha^{k,\mathrm{eq}} &= N_k \boldsymbol{u},\\
\sum_\alpha \boldsymbol{e}_\alpha \boldsymbol{e}_\alpha f_\alpha^{k,\mathrm{eq}} &= c_s^2 N_k \boldsymbol{I} + N_k \boldsymbol{u}\boldsymbol{u},\\
\sum_\alpha F_\alpha^{N,k} &= 0,\\
\sum_\alpha \boldsymbol{e}_\alpha F_\alpha^{N,r} &= 2c_s^2\beta \frac{N_r N_b}{N_r+N_b}\boldsymbol{n},\\
\sum_\alpha \boldsymbol{e}_\alpha F_\alpha^{N,b} &= -2c_s^2\beta \frac{N_r N_b}{N_r+N_b}\boldsymbol{n},\\
\sum_\alpha \boldsymbol{e}_\alpha \boldsymbol{e}_\alpha F_\alpha^{N,k} &= 0.
\end{aligned} \tag{A1}$$

We now proceed in the same manner as discussed in [56] by the following expansion

$$\begin{aligned}
f_\alpha^k &= f_\alpha^{k(0)} + \epsilon f_\alpha^{k(1)} + \epsilon^2 f_\alpha^{k(2)} + \cdots,\\
\partial_t &= \epsilon\partial_{t1} + \epsilon^2\partial_{t2},\\
\boldsymbol{\nabla} &= \epsilon\boldsymbol{\nabla}_1,\\
\boldsymbol{n} &= \epsilon\boldsymbol{n}_1,\\
F_\alpha^{N,k} &= \epsilon F_\alpha^{N,k(1)}.
\end{aligned} \tag{A2}$$

The unit normal vector utilizes the gradient operator which is expanded as $\boldsymbol{\nabla} = \epsilon\boldsymbol{\nabla}_1$; as a result the expanded unit normal vector is $\boldsymbol{n} = \epsilon\boldsymbol{n}_1$ [40]. Based on Eqs. (A1) and (A2),

$$\begin{aligned}
\sum_\alpha f_\alpha^{k(m)} &= 0 \quad (m \geqslant 1),\\
\sum_\alpha F_\alpha^{N,k(1)} &= 0,\\
\sum_\alpha \boldsymbol{e}_\alpha F_\alpha^{N,r(1)} &= 2c_s^2\beta \frac{N_r N_b}{N_r+N_b}\boldsymbol{n}_1,\\
\sum_\alpha \boldsymbol{e}_\alpha F_\alpha^{N,b(1)} &= -2c_s^2\beta \frac{N_r N_b}{N_r+N_b}\boldsymbol{n}_1,\\
\sum_\alpha \boldsymbol{e}_\alpha \boldsymbol{e}_\alpha F_\alpha^{N,k(1)} &= 0.
\end{aligned} \tag{A3}$$

Taylor expansion of Eq. (6) around $\boldsymbol{x}$ and t is applied, so we obtain

$$\begin{aligned}
&D_\alpha f_\alpha^k + \frac{\delta t}{2} D_\alpha^2 f_\alpha^k + \cdots\\
&\quad = -\frac{1}{\tau^N \delta t}\left(f_\alpha^k - f_\alpha^{k,\mathrm{eq}}\right) + \left(\frac{2\tau^N - 1}{2\tau^N}\right) F_\alpha^{N,k},
\end{aligned} \tag{A4}$$

where $D_\alpha = \partial t + \boldsymbol{e}_\alpha \cdot \boldsymbol{\nabla}$. Substituting Eq. (A2) into Eq. (A4) generates the following equations at orders of ϵ^0, ϵ^1, and ϵ^2, respectively:

$$O(\epsilon^0): \quad f_\alpha^{k(0)} = f_\alpha^{k,\mathrm{eq}}, \tag{A5a}$$

$$O(\epsilon^1): \quad D_{1\alpha} f_\alpha^{k(0)} = -\frac{1}{\tau^N \delta t} f_\alpha^{k(1)} + \delta t \left(\frac{2\tau^N - 1}{2\tau^N}\right) F_\alpha^{N,k(1)}, \tag{A5b}$$

$$O(\epsilon^2): \quad \partial_{t2} f_\alpha^{k(0)} + D_{1\alpha} f_\alpha^{k(1)} + \frac{\delta t}{2} D_{1\alpha}^2 f_\alpha^{k(0)} = -\frac{1}{\tau^N \delta t} f_\alpha^{k(2)}, \tag{A5c}$$

where $D_{1\alpha} = \partial t_1 + \boldsymbol{e}_\alpha \cdot \boldsymbol{\nabla}_1$. Summing over α for $O(\epsilon^1)$ gives us

$$\partial_{t1} N_k + \boldsymbol{\nabla}_1 \cdot (N_k \boldsymbol{u}) = 0, \tag{A6}$$

and similarly by substituting Eq. (A5b) into Eq. (A5c) and summing over α for $O(\epsilon^1)$ we obtain

$$\partial_{t2} N_k + \left(\frac{2\tau^N - 1}{2\tau^N}\right)\left\{\boldsymbol{\nabla}_1 \cdot \sum_\alpha \boldsymbol{e}_\alpha f_\alpha^{k(1)} + \frac{\delta t}{2}\boldsymbol{\nabla}_1 \cdot \left[c_s^2 \boldsymbol{n}_1\right]\right\} = 0. \tag{A7}$$

Equations (A1), (A3), and (A5a) have been used in the derivation of Eqs. (A6) and (A7). We can use Eq. (A5b) to obtain the first-order moment of $f_\alpha^{k(1)}$ in Eq. (A7):

$$\begin{aligned}
\sum_\alpha \boldsymbol{e}_\alpha f_\alpha^{r(1)} = -\tau^N \delta t \Bigg[& c_s^2 \boldsymbol{\nabla}_1 N_r - \left(\frac{2\tau^N - 1}{2\tau^N}\right)\\
& \times 2c_s^2\beta \frac{N_r N_b}{N_r+N_b}\boldsymbol{n}_1\Bigg],
\end{aligned} \tag{A8a}$$

$$\begin{aligned}
\sum_\alpha \boldsymbol{e}_\alpha f_\alpha^{b(1)} = -\tau^N \delta t \Bigg[& c_s^2 \boldsymbol{\nabla}_1 N_b + \left(\frac{2\tau^N - 1}{2\tau^N}\right)\\
& \times 2c_s^2\beta \frac{N_r N_b}{N_r+N_b}\boldsymbol{n}_1\Bigg].
\end{aligned} \tag{A8b}$$

Substituting Eq. (A8a) into Eq. (A7) gives us

$$\partial_{t2} N_r = \boldsymbol{\nabla}_1 \cdot \left[\left(\tau^N - \frac{1}{2}\right)\delta t c_s^2 \left(\boldsymbol{\nabla}_1 N_r - 2\beta \frac{N_r N_b}{N_r+N_b}\boldsymbol{n}_1\right)\right], \tag{A9a}$$

$$\partial_{t2} N_b = \boldsymbol{\nabla}_1 \cdot \left[\left(\tau^N - \frac{1}{2}\right)\delta t c_s^2 \left(\boldsymbol{\nabla}_1 N_b + 2\beta \frac{N_r N_b}{N_r+N_b}\boldsymbol{n}_1\right)\right]. \tag{A9b}$$

Multiplying Eqs. (A6) by ϵ and (A9) by ϵ^2 and then summing them lead to

$$\frac{\partial N_r}{\partial t} + \nabla \cdot (N_r \boldsymbol{u}) = D\nabla^2 N_r - 2D\beta\nabla \cdot \left(\frac{N_r N_b}{N_r + N_b}\boldsymbol{n}\right), \tag{A10a}$$

$$\frac{\partial N_b}{\partial t} + \nabla \cdot (N_b \boldsymbol{u}) = D\nabla^2 N_b + 2D\beta\nabla \cdot \left(\frac{N_r N_b}{N_r + N_b}\boldsymbol{n}\right), \tag{A10b}$$

in which the expansion in Eq. (A2) has been used.

APPENDIX B

The incompressible Navier-Stokes equations for multiphase fluid flows are

$$\nabla \cdot \boldsymbol{u} = 0 \tag{B1}$$

and

$$\rho\left(\frac{\partial \boldsymbol{u}}{\partial t} + \boldsymbol{u} \cdot \nabla \boldsymbol{u}\right) = -\nabla p + \nabla \cdot [\eta(\nabla \boldsymbol{u} + (\nabla \boldsymbol{u})^T)] + \boldsymbol{F}_s + \boldsymbol{F}_b + \boldsymbol{F}_a. \tag{B2}$$

[1] G. M. Whitesides, The origins and the future of microfluidics, Nature (London) **442**, 368 (2006).

[2] M. Singh, H. M. Haverinen, P. Dhagat, and G. E. Jabbour, Inkjet printing–process and its applications, Adv. Mater. **22**, 673 (2010).

[3] M. J. Blunt, *Multiphase Flow in Permeable Media: A Pore-Scale Perspective* (Cambridge University Press, Cambridge, 2017).

[4] M. Sahimi, *Flow and Transport in Porous Media and Fractured Rock: From Classical Methods to Modern Approaches* (John Wiley & Sons, New York, 2011).

[5] M. E. Boot-Handford, J. C. Abanades, E. J. Anthony, M. J. Blunt, S. Brandani, N. Mac Dowell, J. R. Fernández, M.-C. Ferrari, R. Gross, J. P. Hallett *et al.*, Carbon capture and storage update, Energy Environ. Sci. **7**, 130 (2014).

[6] R. Scardovelli and S. Zaleski, Direct numerical simulation of free-surface and interfacial flow, Annu. Rev. Fluid Mech. **31**, 567 (1999).

[7] D. M. Anderson, G. B. McFadden, and A. A. Wheeler, Diffuse-interface methods in fluid mechanics, Annu. Rev. Fluid Mech. **30**, 139 (1998).

[8] T. Krüger, H. Kusumaatmaja, A. Kuzmin, O. Shardt, G. Silva, and E. M. Viggen, *The Lattice Boltzmann Method* (Springer, Berlin, 2017).

[9] R. Haghani, A. Fakhari, and M. H. Rahimian, Numerical simulation of three-component multiphase flows at high density and viscosity ratios using lattice Boltzmann methods, Phys. Rev. E **97**, 033312 (2018).

[10] R. Haghani and M.-H. Rahimian, Axisymmetric lattice Boltzmann model for simulation of ternary fluid flows, Acta Mechanica **231**, 2323 (2020).

[11] A. K. Gunstensen, D. H. Rothman, S. Zaleski, and G. Zanetti, Lattice Boltzmann model of immiscible fluids, Phys. Rev. A **43**, 4320 (1991).

[12] X. Shan and H. Chen, Lattice Boltzmann model for simulating flows with multiple phases and components, Phys. Rev. E **47**, 1815 (1993).

[13] X. Shan and G. Doolen, Multicomponent lattice-Boltzmann model with interparticle interaction, J. Stat. Phys. **81**, 379 (1995).

[14] M. R. Swift, W. R. Osborn, and J. M. Yeomans, Lattice Boltzmann simulation of nonideal fluids, Phys. Rev. Lett. **75**, 830 (1995).

[15] X. He, S. Chen, and R. Zhang, A lattice Boltzmann scheme for incompressible multiphase flow and its application in simulation of Rayleigh-Taylor instability, J. Comput. Phys. **152**, 642 (1999).

[16] D. H. Rothman and J. M. Keller, Immiscible cellular-automaton fluids, J. Stat. Phys. **52**, 1119 (1988).

[17] D. Grunau, S. Chen, and K. Eggert, A lattice Boltzmann model for multiphase fluid flows, Phys. Fluids **5**, 2557 (1993).

[18] S. V. Lishchuk, C. M. Care, and I. Halliday, Lattice Boltzmann algorithm for surface tension with greatly reduced microcurrents, Phys. Rev. E **67**, 036701 (2003).

[19] M. Latva-Kokko and D. H. Rothman, Diffusion properties of gradient-based lattice Boltzmann models of immiscible fluids, Phys. Rev. E **71**, 056702 (2005).

[20] T. Reis and T. N. Phillips, Lattice Boltzmann model for simulating immiscible two-phase flows, J. Phys. A: Math. Theor. **40**, 4033 (2007).

[21] H. Liu, A. J. Valocchi, and Q. Kang, Three-dimensional lattice Boltzmann model for immiscible two-phase flow simulations, Phys. Rev. E **85**, 046309 (2012).

[22] Q. Li, K. Luo, Q. Kang, Y. He, Q. Chen, and Q. Liu, Lattice Boltzmann methods for multiphase flow and phase-change heat transfer, Prog. Energy Combust. Sci. **52**, 62 (2016).

[23] H. Huang, J.-J. Huang, X.-Y. Lu, and M. C. Sukop, On simulations of high-density ratio flows using color-gradient multiphase lattice Boltzmann models, Int. J. Mod. Phys. C **24**, 1350021 (2013).

[24] Q. Li, K. H. Luo, Y. L. He, Y. J. Gao, and W. Q. Tao, Coupling lattice Boltzmann model for simulation of thermal flows on standard lattices, Phys. Rev. E **85**, 016710 (2012).

[25] Y. Ba, H. Liu, Q. Li, Q. Kang, and J. Sun, Multiple-relaxation-time color-gradient lattice Boltzmann model for simulating two-phase flows with high density ratio, Phys. Rev. E **94**, 023310 (2016).

[26] Z. X. Wen, Q. Li, Y. Yu, and K. H. Luo, Improved three-dimensional color-gradient lattice Boltzmann model for immiscible two-phase flows, Phys. Rev. E **100**, 023301 (2019).

[27] T. Lafarge, P. Boivin, N. Odier, and B. Cuenot, Improved color-gradient method for lattice Boltzmann modeling of two-phase flows, Phys. Fluids **33**, 082110 (2021).

[28] T. Akai, B. Bijeljic, and M. J. Blunt, Wetting boundary condition for the color-gradient lattice Boltzmann method: Validation with analytical and experimental data, Adv. Water Resour. **116**, 56 (2018).

[29] M. Latva-Kokko and D. H. Rothman, Static contact angle in lattice Boltzmann models of immiscible fluids, Phys. Rev. E **72**, 046701 (2005).

[30] A. Montessori, M. Lauricella, N. Tirelli, and S. Succi, Mesoscale modelling of near-contact interactions for complex flowing interfaces, J. Fluid Mech. **872**, 327 (2019).

[31] A. Montessori, M. Lauricella, A. Tiribocchi, and S. Succi, Modeling pattern formation in soft flowing crystals, Phys. Rev. Fluids **4**, 072201(R) (2019).
[32] I. Halliday, A. P. Hollis, and C. M. Care, Lattice Boltzmann algorithm for continuum multicomponent flow, Phys. Rev. E **76**, 026708 (2007).
[33] A. Subhedar, Color-gradient lattice boltzmann model for immiscible fluids with density contrast, Phys. Rev. E **106**, 045308 (2022).
[34] A. Fakhari, T. Mitchell, C. Leonardi, and D. Bolster, Improved locality of the phase-field lattice-Boltzmann model for immiscible fluids at high density ratios, Phys. Rev. E **96**, 053301 (2017).
[35] J. E. McClure, Z. Li, M. Berrill, and T. Ramstad, The LBPM software package for simulating multiphase flow on digital images of porous rocks, Comput, Geosci. **25**, 871 (2021).
[36] P.-H. Chiu and Y.-T. Lin, A conservative phase field method for solving incompressible two-phase flows, J. Comput. Phys. **230**, 185 (2011).
[37] W. J. Boettinger, J. A. Warren, C. Beckermann, and A. Karma, Phase-field simulation of solidification, Annu. Rev. Mater. Res. **32**, 163 (2002).
[38] Y. Q. Zu and S. He, Phase-field-based lattice Boltzmann model for incompressible binary fluid systems with density and viscosity contrasts, Phys. Rev. E **87**, 043301 (2013).
[39] Y. P. Sitompul and T. Aoki, A filtered cumulant lattice Boltzmann method for violent two-phase flows, J. Comput. Phys. **390**, 93 (2019).
[40] R. Haghani, A. Fakhari, and M.-H. Rahimian, Phase-change modeling based on a novel conservative phase-field method, J. Comput. Phys. **432**, 110111 (2021).
[41] P. Lallemand and L.-S. Luo, Theory of the lattice Boltzmann method: dispersion, dissipation, isotropy, Galilean invariance, and stability, Phys. Rev. E **61**, 6546 (2000).
[42] Q. Li, K. H. Luo, Y. J. Gao, and Y. L. He, Additional interfacial force in lattice Boltzmann models for incompressible multiphase flows, Phys. Rev. E **85**, 026704 (2012).
[43] J. Brackbill, D. Kothe, and C. Zemach, A continuum method for modeling surface tension, J. Comput. Phys. **100**, 335 (1992).
[44] J. Kim, Phase field computations for ternary fluid flows, Comput. Methods Appl. Mech. Eng. **196**, 4779 (2007).
[45] A. Fakhari, D. Bolster, and L.-S. Luo, A weighted multiple-relaxation-time lattice Boltzmann method for multiphase flows and its application to partial coalescence cascades, J. Comput. Phys. **341**, 22 (2017).
[46] M. Geier, A. Fakhari, and T. Lee, Conservative phase-field lattice Boltzmann model for interface tracking equation, Phys. Rev. E **91**, 063309 (2015).
[47] S. T. Zalesak, Fully multidimensional flux-corrected transport algorithms for fluids, J. Comput. Phys. **31**, 335 (1979).
[48] A. Fakhari, M. Geier, and D. Bolster, A simple phase-field model for interface tracking in three dimensions, Comput. Math. Appl. **78**, 1154 (2016).
[49] W. J. Rider and D. B. Kothe, Reconstructing volume tracking, J. Comput. Phys. **141**, 112 (1998).
[50] T. Lee and P. F. Fischer, Eliminating parasitic currents in the lattice Boltzmann equation method for nonideal gases, Phys. Rev. E **74**, 046709 (2006).
[51] R. Haghani, M. H. Rahimian, and A. Fakhari, Conservative phase-field lattice-Boltzmann model for ternary fluids, J. Comput. Phys. **374**, 668 (2018).
[52] F. Ren, B. Song, M. C. Sukop, and H. Hu, Improved lattice Boltzmann modeling of binary flow based on the conservative Allen-Cahn equation, Phys. Rev. E **94**, 023311 (2016).
[53] J. Y. Shao and C. Shu, A hybrid phase field multiple relaxation time lattice Boltzmann method for the incompressible multiphase flow with large density contrast, Int. J. Numer. Methods Fluids **77**, 526 (2015).
[54] T. Lee and C.-L. Lin, A stable discretization of the lattice Boltzmann equation for simulation of incompressible two-phase flows at high density ratio, J. Comput. Phys. **206**, 16 (2005).
[55] C. Josserand and S. Zaleski, Droplet splashing on a thin liquid film, Phys. Fluids **15**, 1650 (2003).
[56] S. Succi, *The Lattice Boltzmann Equation for Fluid Dynamics and Beyond* (Oxford University Press, Oxford, 2001).